The Astrophysical Journal, 785:16 (11pp), 2014 April 10 doi:10.1088/0004-637X/785/1/16

SPATIALLY RESOLVED EMISSION OF A HIGH-REDSHIFT DLA GALAXY WITH THE KECK/OSIRIS IFU*

Regina A. Jorgenson[1] and Arthur M. Wolfe[2]
[1] Institute for Astronomy, University of Hawaii, 2680 Woodlawn Drive, Honolulu, HI, 96822, USA; raj@ifa.hawaii.edu
[2] Department of Physics and Center for Astrophysics and Space Sciences, University of California, San Diego, 9500 Gilman Drive, La Jolla, CA 92093-0424, USA
Received 2013 October 18; accepted 2014 February 10; published 2014 March 21

ABSTRACT

We present the first Keck/OSIRIS infrared IFU observations of a high-redshift damped Lyα (DLA) galaxy detected in the line of sight to a background quasar. By utilizing the Laser Guide Star Adaptive Optics to reduce the quasar point-spread function to FWHM $\sim 0\farcs15$, we were able to search for and map the foreground DLA emission free from the quasar contamination. We present maps of the Hα and [O III] $\lambda\lambda$5007, 4959 emission of DLA 2222−0946 at a redshift of $z \sim 2.35$. From the composite spectrum over the Hα emission region, we measure a star formation rate of $9.5 \pm 1.0\,M_\odot\ \mathrm{yr}^{-1}$ and a dynamical mass of $M_{\rm dyn} = 6.1 \times 10^9\,M_\odot$. The average star formation rate surface density is $\langle\Sigma_{\rm SFR}\rangle = 0.55\,M_\odot\ \mathrm{yr}^{-1}\ \mathrm{kpc}^{-2}$, with a central peak of $1.7\,M_\odot\ \mathrm{yr}^{-1}\ \mathrm{kpc}^{-2}$. Using the standard Kennicutt–Schmidt relation, this corresponds to a gas mass surface density of $\Sigma_{\rm gas} = 243\,M_\odot\ \mathrm{pc}^{-2}$. Integrating over the size of the galaxy, we find a total gas mass of $M_{\rm gas} = 4.2 \times 10^9\,M_\odot$. We estimate the gas fraction of DLA 2222−0946 to be $f_{\rm gas} \sim 40\%$. We detect [N II] λ6583 emission at 3σ significance with a flux corresponding to a metallicity of 75% solar. Comparing this metallicity with that derived from the low-ion absorption gas ∼6 kpc away, ∼30% solar, indicates possible evidence for a metallicity gradient or enriched in/outflow of gas. Kinematically, both Hα and [O III] emission show relatively constant velocity fields over the central galactic region. While we detect some red and blueshifted clumps of emission, they do not correspond with rotational signatures that support an edge-on disk interpretation.

Key words: cosmology: observations – galaxies: formation – galaxies: high-redshift – intergalactic medium – quasars: absorption lines – quasars: individual (SDSS J222256.11–094636.2)

Online-only material: color figures

1. INTRODUCTION

The emerging picture of galaxy formation and evolution at high redshift is currently dominated by observations of the star formation rate per unit comoving volume from $z \gtrsim 7$ to the present day, and shows that 50% of the current stellar mass of galaxies formed in the redshift interval $1.5 < z < 3.5$ (Reddy & Steidel 2009). Photometric surveys for galaxies have succeeded in tracing their stellar content out to redshifts as large as 6 or higher (Ellis et al. 2013; Lehnert et al. 2010; Giavalisco et al. 2004; Bouwens et al. 2004). The majority of galaxies found in this way are the Lyman break galaxies (LBGs; e.g., Steidel et al. 2003), which are selected for bright rest-frame UV emission. These are star-forming (mean SFR $\sim 40\,M_\odot\ \mathrm{yr}^{-1}$) galaxies with average half-light radii $\langle r_{1/2}\rangle \approx 2$ kpc (Shapley et al. 2004). Because they are strongly clustered ($r_0 \approx 4\ h^{-1}$ Mpc; Adelberger et al. 2005), the LBGs are likely to be biased tracers of dark-matter halos with masses $M_{\rm DM} \sim 10^{+12}\,M_\odot$. Consequently, the LBGs were originally thought to be the progenitors of massive elliptical galaxies (Steidel et al. 1999, 2003). However, recent studies of Hα emission at $z \approx 2.5$ with the SINFONI IFU on the Very Large Telescope (VLT) and OSIRIS on Keck suggest some fraction could be the progenitors of massive spiral galaxies. This follows from the detection of disks rotating with circular velocities $v_c \approx 200$ to 250 km s^{-1} (Law et al. 2012; Förster Schreiber et al. 2009a; Genzel et al. 2006).

The possibility that massive spirals were in place at $z > 2$ has important implications for hierarchical theories of galaxy formation, which predict most objects at $z > 2$ to have $v_c \ll 250$ km s^{-1}. In addition, the link between massive, high star formation rate LBGs, and the neutral atomic gas that must be the fuel for their copious star formation remains unclear. Recent models have connected the Lyα (DLA) absorption systems, another class of high-z objects that qualify as spiral progenitors, with the LBGs (Wolfe et al. 2008). The DLAs are drawn from a cross-section weighted sample of neutral gas layers, which contain sufficient neutral gas to account for most of the visible stars in modern galaxies, and with properties resembling those of spiral disks (Wolfe et al. 2005). Interestingly, the DLA absorption-line kinematics are consistent with randomly oriented disks with $v_c \approx 250$ km s^{-1}. However, since the velocity fields are deduced from absorption-line studies alone, the DLA masses and sizes are generally unknown. However, Cooke et al. (2005, 2006) cross-correlate DLAs with LBGs at $z \sim 3$ and find that they reside in similar spatial locations and have a similar inferred dark matter halo mass range of $10^{9-12}\,M_\odot$. Alternate models have suggested that DLA velocity profiles are consistent with merging protogalactic clumps of gas predicted by smoothed particle hydrodynamics simulations of structure formation (Haehnelt et al. 1998; Hong et al. 2010; however, see Prochaska & Wolfe 2010 who point out several mistreatments in these works).

Despite evidence for star formation (Wolfe et al. 2003) and metal enrichment (Rafelski et al. 2012; Jorgenson et al. 2013a) in DLAs, the direct detection of DLAs in emission has been rare. Efforts to image DLAs directly have generally been unsuccessful because of the difficulty of detecting relatively faint foreground emission near a much brighter background quasar

* The data presented herein were obtained at the W. M. Keck Observatory, which is operated as a scientific partnership among the California Institute of Technology, the University of California and the National Aeronautics and Space Administration. The Observatory was made possible by the generous financial support of the W. M. Keck Foundation.

(i.e., Lowenthal et al. 1995; Bunker et al. 1999; Kulkarni et al. 2000, 2006; Christensen et al. 2009 and several unpublished works). To date, only 11 $z > 2$ DLAs have been detected in emission (see Krogager et al. 2012 for a summary and Schulze et al. 2012 for an additional detection in a GRB-DLA). Most of these targets were detected in single slit observations, requiring fortuitous slit placement and providing limited information on the total fluxes, star formation rates (SFRs) and kinematics of the emission.

The advent of Laser Guide Star Adaptive Optics (LGSAO) corrected Integral Field Units (IFU) on 10 m class telescopes, such as the Keck/OSIRIS IFU (Larkin et al. 2006), creates a clear, new path forward to answering some questions raised since the first surveys of DLAs (Wolfe et al. 1986). By taking advantage of the LGSAO correction to minimize the point-spread function (PSF) of the background quasar, it is possible to search for DLA emission at small impact parameters while simultaneously obtaining spectra that provide mass and kinematic measures. Will a majority of high-z DLAs reveal disk-like rotation, further challenging the hierarchical theory of structure formation? Are star formation rates as estimated by the C II* technique (Wolfe et al. 2003) and implying that ∼50% of DLAs should be associated with the halos of LBGs (Wolfe et al. 2008) correct? Only by complementing the wealth of DLA absorption-line data with the direct detection and mapping of emission can the true nature of these enigmatic systems be understood.

We have used the Keck/OSIRIS IFU with LGSAO to target the high metallicity DLA, DLA 2222−0946, first found by Fynbo et al. (2010) to have relatively strong Lyα, Hα, and [O III] λ4959, λ5007 emission in single-slit VLT/X-Shooter observations. At a redshift of $z \sim 2.35$, DLA 2222−0946 has a neutral hydrogen gas column density of $N_{\rm H\,I} = 4.5 \times 10^{20}$ cm^{-2}, a metallicity of [M/H][3] ~ -0.5 (Krogager et al. 2013; Jorgenson et al. 2013a) and lies along the line of sight to the background quasar SDSS J222256.11−094636.2.

DLA 2222−0946 was imaged with the VLT/SINFONI IFU by Péroux et al. (2012) and then again by Peroux et al. (2013), however in both cases only Natural Guide Star Adaptive Optics (NGSAO) was used, leading to PSFs of FWHM = 0.″6 and FWHM = 0.″4, respectively. At the redshift of the DLA, this PSF corresponds to ∼4 kpc, which could very easily mask kinematic signatures in a compact galaxy (e.g., Newman et al. 2013). In addition, Péroux et al. (2012) and Peroux et al. (2013) only targeted Hα emission, while the [O III] flux is measured to be stronger from single slit observations (Fynbo et al. 2010). Krogager et al. (2013) used the *Hubble Space Telescope* (*HST*) to image the stellar continuum of DLA 2222−0946 in the rest-frame optical-UV regime and estimate the SFR, stellar and dynamical masses, and morphology. From the *HST* imaging Krogager et al. (2013) conclude that the galaxy has a compact yet elongated morphology indicative of a galactic disk viewed edge-on.

In this paper, we present the first observations of a high-redshift DLA in emission utilizing the Keck/OSIRIS IFU and LGSAO. We detect and map the flux and velocity field of DLA 2222−0946 in both Hα and [O III] emission with a PSF of FWHM ∼ 0.″15. While we find interesting morphological and kinematical signatures, we find no evidence of ordered edge-on disk rotation.

[3] We use the standard shorthand notation for metallicity relative to solar, $[{\rm M/H}] = \log({\rm M/H}) - \log({\rm M/H})_\odot$.

The paper is organized as follows. We describe our observations and data reduction process in Section 2. In Section 3, we discuss the details of the analysis of the final data cube. We attempt to place these results in a larger context in Section 4, before summarizing in Section 5. Throughout the paper, we assume a standard lambda cold dark matter (ΛCDM) cosmology based on the final 9 yr *Wilkinson Microwave Anisotropy Probe* results (Hinshaw et al. 2013) in which $H_0 = 70.0$ km s^{-1} Mpc^{-1}, $\Omega_m = 0.279$, and $\Omega_\Lambda = 0.721$.

2. OBSERVATIONS

Observations were performed using the OSIRIS (Larkin et al. 2006) infrared integral-field spectrograph in combination with the Keck I LGSAO system during two half-nights on 2012 July 20 and 21. We utilized two narrow-band filters, Hn4 and Kn3, corresponding to the redshifted wavelengths of [O III] and Hα emission from DLA 2222−09, respectively. In order to achieve the best compromise between maximizing the field of view and spatial resolution, we chose the 50 mas plate scale, which provides fields of view of 2.″1 × 3.″2 and 2.″4 × 3.″2 for the Hn4 and Kn3 filters, respectively. The spectral resolution varies from spatial pixel to spatial pixel (spaxel), but is approximately $R \sim 3600$, as confirmed by measures of the average FWHM of a series of OH-sky lines.

Exposure times were 900 s. In order to maximize the on-source exposure time, rather than obtaining an off-source skyframe, we utilized an A-B observing pattern in which the target was placed in the top half of the field of view for frame A and then shifted to the bottom half of the field of view for frame B. We then used observation B as the sky frame for observation A and vice versa. In this way we cut our field of view in half, but doubled our on-source observing time. This procedure ensured the maximum probability for detecting faint extended emission and was particularly useful given that we already had an idea of the position of the emission from previous works (Fynbo et al. 2010; Péroux et al. 2012; Krogager et al. 2013). A suitable, bright ($R < 17$) star within 50″ of the target was used for tip tilt correction. All observations were taken in clear weather with good, ∼0.″6 or better, seeing.

Over the course of two half nights we obtained 14 × 900 s in the Hn4 band and 12 × 900 s in the Kn3 band for total exposure times of 3.5 hr and 3 hr for the [O III] and Hα emission, respectively.

2.1. Data Reduction and Flux Calibration

Data reduction was performed using a combination of the Keck/OSIRIS data reduction pipeline (DRP) and custom IDL routines in a process similar to that outlined in Law et al. (2007) and Law et al. (2009). We used the DRP to perform the standard reduction and extraction of the three-dimensional data cubes, including the `Scaled Sky Subtraction` Module. In order to mitigate the effects of highly variable sky lines, we performed a second-pass sky subtraction using custom IDL routines to calculate the median pixel value in each spectral channel and subtract this value from all pixels within the channel to ensure a zero-flux median in all spectral slices throughout the data cube. Because the galaxy and background quasar are in each frame as both a positive and a negative, they contribute net-zero to the median flux.

We then applied a telluric correction to each science frame, using the telluric standard star taken closest in time to the science frame. In order to flux calibrate the data, we used the telluric

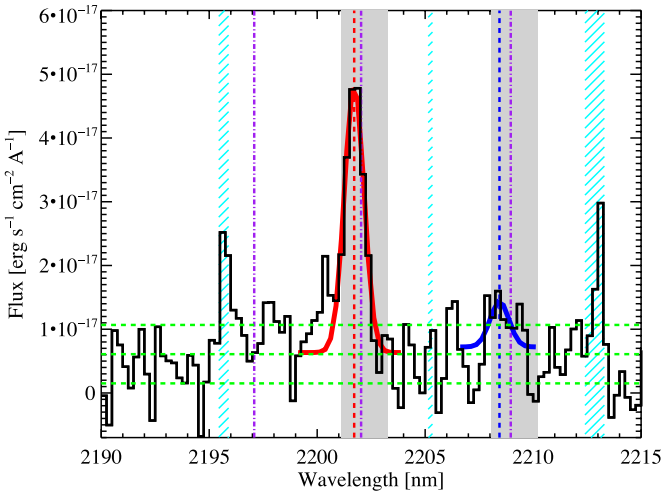

Figure 1. Composite spectrum over an ∼0.″5 × 0.″5 region centered on the peak of Hα emission. The Hα emission is shown here with a best-fit Gaussian overlaid in red, while the best-fit Gaussian to the [N II] λ6583 is shown in blue. The best-fit redshift of the Hα emission is $z = 2.35391$, indicated here by the vertical red dashed line. This can be compared with the fiducial absorption-line redshift, $z_{\rm HIRES} = 2.35440$, indicated here by the purple dash-dot lines. The gray vertical regions indicate the entire redshift range of the low-ion absorption. Cyan hashed regions indicate the locations of strong atmospheric OH emission features which can leave residuals.

(A color version of this figure is available in the online journal.)

standard star and a reference Vega spectrum. As discussed by Law et al. (2009), the uncertainty in the absolute flux calibration of LGSAO data is estimated to be ∼30% due primarily to rapid and potentially significant fluctuations of the AO-corrected core of the PSF.

In order to produce a final data cube, we took advantage of the fact that each frame contains the relatively bright image of the quasar, and we used the peak emission of the quasar to align the frames for mosaicing. We produced the final data cube using the OSIRIS module `Mosaic Frames` and an input file containing the frame offsets determined from the quasar centroid in each frame. The frames were combined using the sigma-clipping average routine, `meanclip`. Given our observing method of keeping the quasar and DLA in every frame, the final data cube consists of a positive central region with negative regions above and below. In the final analysis, we considered only spaxels located in the central positive region.

Gaussian fits to the PSF of the quasar in the mosaiced image yield FWHM ∼ 3.0 and FWHM ∼ 3.4 pixels for the K and *H* bands, respectively. For the 50 mas pixel scale, this corresponds to a FWHM of ∼0.″15 and ∼0.″17, respectively. In order to enhance the detail of the relatively faint emission, we spatially resampled the data to 0.″025 pixel^{-1} and then smoothed with a Gaussian kernel with FWHM = 0.″15, similar to that of the LGSAO PSF.

Finally, we used the IRAF package `rvcorrect` to correct the spectra for the heliocentric motion of the earth such that all wavelengths and redshifts are reported in the heliocentric vacuum frame. Redshifts were determined using the rest-frame vacuum wavelengths of Hα, [O III], and [N II] (i.e., 6564.614 Å, 5008.239 Å, and 6585.27 Å, respectively). We checked the spectral resolution by measuring the FWHM of OH-skylines in the vicinity of the redshifted Hα and [O III] emission-lines and confirmed that the average resolution corresponds to $R \sim 3600$, or FWHM ∼ 83 km s^{-1}. The reported velocity dispersions have been corrected for the instrumental FWHM (FWHM$_{\rm instrumental}$ ∼ 83 km s^{-1}) by subtracting it in quadrature.

Table 1
Summary of Hα Flux, Luminosity, and SFR for DLA 2222−09

Author	F(Hα) (erg s^{-1} cm^{-2})	L(Hα) (erg s^{-1})	SFR(Hα) ($M_\odot$ yr^{-1})
This work	$(4.76 \pm 0.50) \times 10^{-17}$	$(2.13 \pm 0.23) \times 10^{42}$	9.5 ± 1.0
F10[a]	2.5×10^{-17}	1.1×10^{42}	10
P12[b]	$(8.7 \pm 2.6) \times 10^{-17}$	$(3.85 \pm 0.11) \times 10^{42}$	17.1 ± 5.1
P13[c]	5.6×10^{-17}	...	...
K13[d]	$(5.7 \pm 0.3) \times 10^{-17}$	$(2.4 \pm 0.10) \times 10^{42}$	$12.7^{e} \pm 0.7$

Notes.
[a] Fynbo et al. (2010).
[b] Péroux et al. (2012).
[c] Peroux et al. (2013), luminosity and SFR not provided.
[d] Krogager et al. (2013).
[e] Using dust extinction derived from their UV data.

3. ANALYSIS

In this section, we describe our analysis of the final OSIRIS data cube, including the derived flux and star formation rate estimates.

3.1. Hα Flux, Luminosity, and Star Formation Rate

We estimate the total detected Hα flux, $F^{\rm H\alpha}$, by summing the spectra in all spaxels in a ∼0.″5 × 0.″5 box centered on the location of the peak Hα emission. This composite spectrum is presented in Figure 1. Fitting a Gaussian to the emission-line provides a total Hα flux of $F^{\rm H\alpha} = (4.76 \pm 0.50) \times 10^{-17}$ erg s^{-1} cm^{-2}, where the error is taken to be the standard deviation in the residual spectrum after subtraction of the Gaussian model. This corresponds to an Hα luminosity of $L^{\rm H\alpha} = (2.13 \pm 0.23) \times 10^{42}$ erg s^{-1}, not corrected for dust. As in Law et al. (2009), we use the Kennicutt et al. (1994) calibration to convert Hα luminosity to SFR,

$$\mathrm{SFR}(M_\odot\ \mathrm{yr}^{-1}) = \frac{L^{\rm H\alpha}}{1.26 \times 10^{41}\ \mathrm{erg\ s}^{-1}} \times 0.56 \qquad (1)$$

assuming a Chabrier (2003) initial mass function. We estimate a SFR $\approx 9.5 \pm 1.0\, M_\odot$ yr^{-1}. This result is consistent, to within errors, of several previous estimates by Fynbo et al. (2010), Péroux et al. (2012), and Krogager et al. (2013). We summarize the Hα measurements in Table 1 to aid in comparison with previous works because all authors used slightly different cosmologies and assumptions to convert Hα flux to SFR.

From the best-fit Gaussian, we estimate a FWHM (Hα) = 144 ± 7 km s^{-1}, or 118 km s^{-1}, with the effects of instrumental smoothing (FWHM$_{\rm instrumental}$ = 83 km s^{-1}) taken out in quadrature. We also estimate the best-fit redshift of the Hα emission-line to be $z = 2.35391$. We note that this redshift is −44 km s^{-1} from $z_{\rm HIRES} = 2.35440$, the redshift of a central, low-ion velocity component with the largest optical depth as measured from an archival Keck/HIRES spectrum. For the purposes of this paper, we will arbitrary define $z_{\rm HIRES}$ to be the fiducial redshift of the system (see Section 4.5 for details). This fairly large and complex absorption-line system contains several velocity components spanning the redshift range $z = 2.3530$ to 2.3563. The centroid of Hα emission falls roughly in the middle of the absorption-line profile which is indicated by the shaded

Table 2
Line Diagnostics of DLA 2222−09

Quantity	Units	Measured
$z_{\rm HIRES}$		2.35440
z(Hα)		2.35391
Δv(Hα)[a]	[km s^{-1}]	−44
FWHM(Hα)	[km s^{-1}]	144 ± 7
FWHM(Hα)[b]	[km s^{-1}]	118
z([N II])		2.35384
Δv([N II])[a]	[km s^{-1}]	−50
FWHM([N II])[c]	[km s^{-1}]	124 ± 32
FWHM([N II])[b]	[km s^{-1}]	92
z([O III] λ5007)		2.35397
Δv([O III] λ5007)[a]	[km s^{-1}]	−39
FWHM([O III] λ5007)	[km s^{-1}]	155 ± 7
FWHM([O III] λ5007)[b]	[km s^{-1}]	131
z([O III] λ4959)		2.35406
Δv([O III] λ4959)[a]	[km s^{-1}]	−30
FWHM([O III] λ4959)	[km s^{-1}]	138 ± 22
FWHM([O III] λ4959)[b]	[km s^{-1}]	111

Notes.
[a] Velocity difference between $z_{\rm HIRES}$ and the given transition.
[b] Effects of instrumental smoothing taken out in quadrature.
[c] Measured from the composite spectrum over the central ∼0.″15 × 015″ shown in Figure 2.

Table 3
Summary of Results for DLA 2222−09

Quantity	Units	Measured
F(Hα)[a]	[erg s^{-1} cm^{-2}]	(4.76 ± 0.50) × 10^{-17}
L(Hα)	[erg s^{-1}]	(2.13 ± 0.23) × 10^{42}
$M_{\rm dyn}$	[$M_\odot$]	6.1 × 10^9
SFR	[$M_\odot$ yr^{-1}]	9.5 ± 1.0
$\langle\Sigma_{\rm SFR}\rangle$	[$M_\odot$ yr^{-1} kpc^{-2}]	0.55
Peak $\Sigma_{\rm SFR}$	[$M_\odot$ yr^{-1} kpc^{-2}]	1.7
$\langle\Sigma_{\rm gas}\rangle$	[$M_\odot$ pc^{-2}]	243
$M_{\rm gas}$	[$M_\odot$]	4.2 × 10^9
$f_{\rm gas}$		∼40%
F([N II])[a]	[erg s^{-1} cm^{-2}]	(1.48 ± 0.46) × 10^{-18}
L([N II])	[erg s^{-1}]	(6.62 ± 2.1) × 10^{40}
12+log(O/H)		8.54 ± 0.14
Metallicity	% of solar	0.75
F([O III] λ5007)[a]	[erg s^{-1} cm^{-2}]	(7.87 ± 0.62) × 10^{-17}
L([O III] λ5007)	[erg s^{-1}]	(3.52 ± 0.28) × 10^{42}
F([O III] λ4959)[a]	[erg s^{-1} cm^{-2}]	(2.91 ± 0.74) × 10^{-17}
L([O III] λ4959)	[erg s^{-1}]	(1.31 ± 0.33) × 10^{42}

Note. [a] 1σ uncertainties are determined after subtraction of the Gaussian model.

grey region in Figure 1. We delay a more detailed comparison between the absorption and emission-line kinematics until Section 4.5. In Table 2, we provide a summary of all line diagnostics, while in Table 3 we summarize the general results.

3.2. [N II]

We report a detection of the [N II] λ6583 emission-line with a significance of 3σ. While we attempt to fit the [N II] emission-line with a Gaussian, shown in blue in Figure 1, we find that the [N II] emission is much more centrally confined than the stronger Hα emission. Therefore, to achieve the most significant detection, we created a spectral stack over only the central ∼0.″15 × 0.″15 where [N II] emission is the strongest, shown in Figure 2. Line fit details are given in Table 2. The

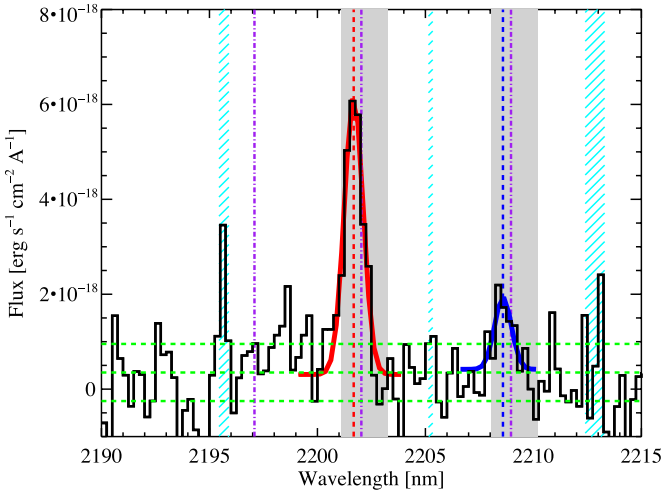

Figure 2. Composite spectrum over the central ∼0.″15 × 0.″15 region centered on the peak of [N II] emission. The [N II] λ6583 emission-line, fit by a Gaussian in blue, is detected at 3σ significance. The security of the line identification is raised by the fact that the independently fit Hα line agrees in redshift with a difference of ∼2 km s^{-1}, well within the errors.
(A color version of this figure is available in the online journal.)

best-fit Gaussian flux measures $F^{\rm [N II]}$ = (1.48 ± 0.46) × 10^{-18} erg s^{-1} cm^{-2} corresponding to a luminosity $L^{\rm [N II]}$ = (6.62 ± 2.1) × 10^{40} erg s^{-1}. Under the assumption that this is a detection, we can use the $N2$ index, where $N2$ is the ratio of [N II] to Hα flux, to estimate the metallicity. We use the Hα flux over this same region, as fit by a Gaussian (red in Figure 2), $F^{\rm H\alpha}$ = (6.38 ± 0.66) × 10^{-18} erg s^{-1} cm^{-2}. As calibrated by Pettini & Pagel (2004), we use the relation 12 + log(O/H) = 8.90 + 0.57 × $N2$ to infer a metallicity of 12 + log(O/H) = 8.54 ± 0.14. Assuming a solar oxygen abundance of 12 + log (O/H) = 8.66 (Asplund et al. 2004), the derived metallicity corresponds to 75% solar metallicity. If we include the 1σ dispersion in the $N2$ relation, 0.18 dex, we find 12 + log(O/H) = 8.54 ± 0.32. The lower range, at ∼40% solar, is just consistent with the metallicity as measured from the absorption-lines, [M/H] = −0.56 ± 0.1, or ∼30% solar (Jorgenson et al. 2013a; Krogager et al. 2013; Fynbo et al. 2010). We can also compare with the emission line metallicity measured by Krogager et al. (2013) using VLT/X-Shooter spectra, ∼50% solar (note that Krogager et al. 2013 use a slightly different oxygen abundance of 8.69, which applied here would result in a slightly lower metallicity of ∼70% solar). As the effective aperture of the Krogager et al. (2013) result is larger, this may indicate, albeit with large uncertainties, evidence of a possible metallicity gradient. We discuss the possibility of a metallicity gradient or the in/outflow of metal-enriched gas in Section 4.4. We also note that over this central ∼0.″15 × 0.″15 region, the independently fit redshifts of the [N II] and Hα emission agree to within ∼2 km s^{-1}, as seen in Figure 2 (i.e., $z_{\rm abs}^{\rm [N II]}$ = 2.35384 and $z_{\rm abs}^{\rm H\alpha}$ = 2.35386).

For completeness we provide the results from fitting the [N II] emission-line taken over the entire ∼0.″5 × 0.″5 region shown in Figure 1. While this line is only significant at the 1.5σ level, the best-fit Gaussian flux measures $F^{\rm [N II]}$ = (7.83 ± 4.69) × 10^{-18} erg s^{-1} cm^{-2} corresponding to a luminosity $L^{\rm [N II]}$ = (3.51 ± 2.1) × 10^{41} erg s^{-1}. Using the Pettini & Pagel (2004) calibrated relation, we find a metallicity of 12 + log(O/H) = 8.45 ± 0.26, corresponding to 62% solar metallicity.

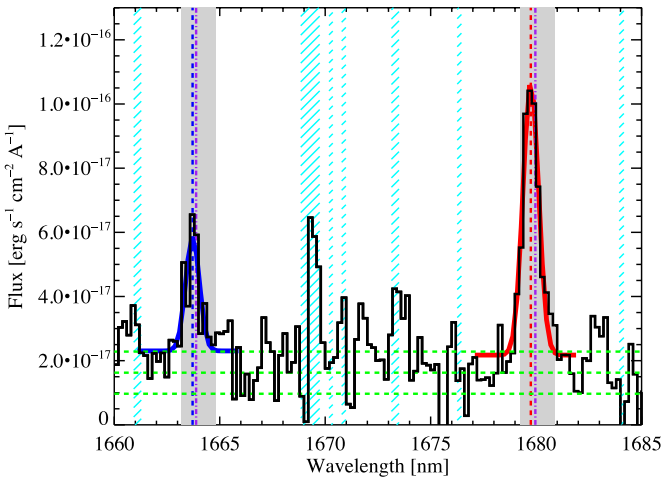

Figure 3. Composite spectrum over an ∼0.″75 × 0.″75 region centered on the peak of [O III] emission. The [O III] λ5007 emission is shown here with the best-fit Gaussian overlaid in red, while the blue fit on the left corresponds to the detection of [O III] λ4959. The redshift of the [O III] λ5007 line is $z = 2.35397$ (red dashed line), which is −39 km s^{-1} from the fiducial absorption-line redshift, $z_{\rm HIRES} = 2.35440$, indicated here by the purple dash-dot lines. The gray vertical regions indicate the entire redshift range of the low-ion absorption. Cyan hashed regions indicate the locations of strong atmospheric OH emission features which can leave residuals.

(A color version of this figure is available in the online journal.)

3.3. [O III] Flux and Luminosity

We estimate the total detected [O III] flux by summing the spectra in all spaxels in a ∼0.″75 × 0.″75 region around the peak [O III] emission. Note that the [O III] emission is stronger and more spatially extended than the Hα emission. We detect both [O III] λ5007 and [O III] λ4959 with high significance, as shown in Figure 3, where we present the composite spectrum. Fitting a Gaussian to the [O III] λ5007 emission (shown in Figure 3, red), we measure a total [O III] flux of $F^{[\rm O\,III]\,\lambda5007} = (7.87 \pm 0.62) \times 10^{-17}$ erg s^{-1} cm^{-2}. This corresponds to an [O III] luminosity of $L^{[\rm O\,III]} = (3.52 \pm 0.28) \times 10^{42}$ erg s^{-1}.

We applied an independent Gaussian fit to the [O III] λ4959 line and measure a total flux, $F^{[\rm O\,III]\,\lambda4959} = (2.91 \pm 0.74) \times 10^{-17}$ erg s^{-1} cm^{-2}. This corresponds to an [O III] luminosity of $L^{[\rm O\,III]} = (1.31 \pm 0.33) \times 10^{42}$ erg s^{-1}. The flux ratio of F([O III] λ5007)/F([O III] λ4959) ≈ 2.7, a slight deviation from the expected [O III] λ5007:[O III] λ4959 = 3:1, is insignificant given the errors in flux determination. We provide all line-fit details in Table 2.

3.4. Spatial Mapping of Intensity, Velocity, Velocity Dispersion, and Signal-to-noise Ratio

In order to map the location of emission and find kinematical signatures, we searched for emission in the spectrum of each spaxel. For each emission-line considered, the fitting method attempted to fit a Gaussian at the expected location of emission and compared the chi-squared result to that of a fit with no emission-line. A detection required a minimum of 1σ to be accepted as a detection. In this way, we created a two-dimensional map of emission for each line, where each spaxel contains a best-fit flux, velocity (relative to the best-fit redshift determined from the composite spectral stack), and velocity dispersion. The reported velocity dispersions have been corrected for the instrumental resolution by subtraction of the instrumental sigma, $\sigma_{\rm instrumental} \sim 35$ km s^{-1}, in quadrature. In cases where there was no line detected, or the signal-to-noise ratio (S/N) was too low we do not report a detection and leave the spaxel black in the final maps.

We present the Hα and [O III] emission maps in Figures 4 and 5, respectively. Each figure contains a relative flux map, centered on the peak emission location (top left), and the corresponding velocity map (bottom left), and velocity dispersion map (bottom right). The average FWHM of the PSF as measured by the image of the quasar (not pictured) is indicated by the white bar, and is FWHM ∼ 0.″15 and FWHM ∼ 0.″20 for the Hα and [O III] maps, respectively. In all maps, the quasar (not pictured) is located at $x \sim 0.''5$ and $y \sim -0.''6$, and indicated by a "Q." The distance from the quasar to the center of the DLA emission is ∼0.″7, corresponding to a physical distance at the redshift of the DLA of ∼5.8 kpc (where 1″ corresponds to ∼8.34 kpc).

In order to gauge the significance of the detected line emission, we calculate the S/N of the line detection in each spaxel by measuring the standard deviation of the noise in a nearby spectral region free from skylines or other emission-lines. We then estimate the S/N as the ratio of the amplitude of the best-fit Gaussian to the standard deviation of the noise region (where the amplitude of the best-fit Gaussian is taken to be the maximum of the Gaussian fit minus the continuum level of the fit). Variations in the S/N from spaxel to spaxel are shown in the upper right panel of Figures 4 and 5.

4. RESULTS

In this section, we discuss the estimates of mass and star formation rate surface density as well as the implications of the derived kinematics of the galaxy.

4.1. Dynamical Mass Estimate

We estimate the dynamical mass of the galaxy within the radius probed by the Hα emission using Equation (2) from Law et al. (2009),

$$M_{\rm dyn} = \frac{C\sigma_{\rm net}^2 r}{G}, \quad (2)$$

where $C = 5$ for a uniform sphere (Erb et al. 2006), and $\sigma_{\rm net} \sim 50$ km s^{-1}, as measured from the stacked Hα spectrum shown in Figure 1. Following the method outlined in Law et al. (2007), we estimate the effective radius r to be 0.″25, which corresponds to ∼2.1 kpc at the redshift of the galaxy. The calculated dynamical mass is therefore $M_{\rm dyn} = 6.1 \times 10^9\ M_\odot$. We can compare this with the dynamical mass derived by Krogager et al. (2013) of $M_{\rm dyn} = 2.5 \times 10^9\ M_\odot$. We note that while Krogager et al. (2013) report a σ value nearly equal to the value reported here ($\sigma \sim 49.1$ km s^{-1}), they measure a smaller galactic size, with semi-major axis $a_e = 1.12$ kpc from their *HST* UV imaging, and as a result estimate a smaller $M_{\rm dyn}$.

We find that the dynamical mass of DLA 2222−09 is slightly larger than that of the Small Magellanic Cloud, measured to be $M_{\rm dyn} = 2.4 \times 10^9\ M_\odot$. Moreover, it is similar to the low end of the dynamical mass range of the high-redshift star forming galaxies studied by Law et al. (2009), which range from $M_{\rm dyn} = 3 \times 10^9\ M_\odot$ to $M_{\rm dyn} = 25 \times 10^9\ M_\odot$.

Given the observational limitations, there are currently few direct measurements of dynamical masses of DLAs reported in the literature. Chengalur & Kanekar (2002) use H I 21 cm imaging to estimate the dynamical mass of a low-redshift DLA, at $z = 0.009$, to be $M_{\rm dyn} = 5 \times 10^9\ M_\odot$, similar to the galaxy presented here. While Péroux et al. (2011) used the VLT/SINFONI IFU to map Hα emission and estimate the

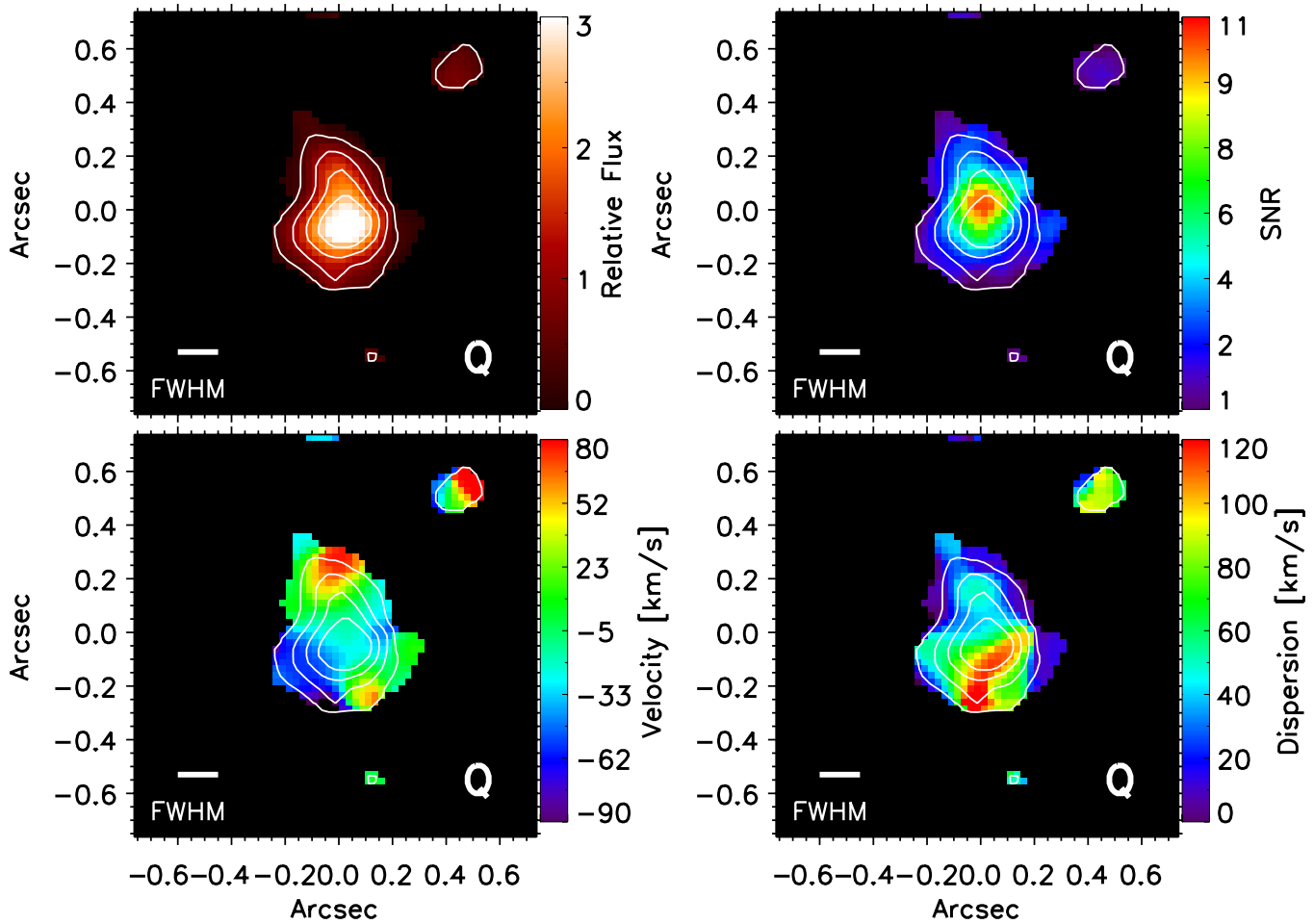

Figure 4. Hα intensity (top left), velocity (bottom left), velocity dispersion (bottom right), and S/N (top right) maps. The orientation is the standard north is up and east is to the left. The velocity is relative to $z = 2.35391$, the best-fit redshift determined from the composite spectrum shown in Figure 1. Individual spaxels are 0.025 arcsec^2. The FWHM = ∼0.″15 of the PSF after smoothing is shown in the lower left corner of the intensity map. At the redshift of the DLA 1″ corresponds to ∼8.3 kpc. The quasar, indicated by a "Q," is located in the lower right-hand corner at approximately $x = 0.''5$ and $y = -0.''6$.

(A color version of this figure is available in the online journal.)

dynamical masses of a DLA and sub-DLA at $z \sim 1$ to be significantly larger at $M_{\rm dyn} = 2.0 \times 10^{10}\,M_\odot$ and $M_{\rm dyn} = 7.9 \times 10^{10}\,M_\odot$, respectively. Recently, Bouché et al. (2013) determined the dynamical mass of a DLA galaxy at $z \sim 2.3$ to be $M_{\rm dyn} = 2.0 \times 10^{10}\,M_\odot$.

4.2. Star Formation Rate Surface Density and Gas Mass Estimates

In order to use the Kennicutt–Schmidt relation (Kennicutt 1998) to estimate the gas mass of the galaxy, we first estimate the star formation rate surface density, $\Sigma_{\rm SFR}$. We do this by calculating the star formation rate, as in Equation (1), in each 0.025 arcsec^2 spaxel, and use the scale 1 arcsec = 8.338 kpc at the redshift of DLA 2222−09 (note: spaxel size is smaller because of oversampling). The $\Sigma_{\rm SFR}$ peaks at the center of the Hα emission, to a maximum value of $\Sigma_{\rm SFR} = 1.7\,M_\odot\,{\rm yr}^{-1}\,{\rm kpc}^{-2}$. We find a mean star formation rate surface density of $\langle\Sigma_{\rm SFR}\rangle = 0.55\,M_\odot\,{\rm yr}^{-1}\,{\rm kpc}^{-2}$. This value is about an order of magnitude lower than the $\Sigma_{\rm SFR}$ found for LBGs of Law et al. (2007). According to the results of Kennicutt (1998), this rate places DLA 2222−09 at the high end of the sample of normal disk galaxies and at the low end of starburst samples.

We use the Kennicutt–Schmidt relation (Kennicutt 1998),

$$\Sigma_{\rm SFR} = (2.5 \pm 0.7) \times 10^{-4} \left(\frac{\Sigma_{\rm gas}}{1\,M_\odot\,{\rm pc}^{-2}}\right)^{1.4\pm0.15}, \quad (3)$$

to calculate the gas mass surface density, $\Sigma_{\rm gas}$. We find a mean gas mass surface density of $\langle\Sigma_{\rm gas}\rangle = 243\,M_\odot\,{\rm pc}^{-2}$. Integrating over the extent of the emission region, we find a total gas mass of $M_{\rm gas} = 4.2 \times 10^9\,M_\odot$. Considering the uncertainties and large inherent errors, our results agree fairly well with those of Krogager et al. (2013) who estimate the gas mass of this galaxy to be $M_{\rm gas} = 1 \times 10^9\,M_\odot$. We find that this gas mass is approximately an order of magnitude less than those of star forming galaxies at $z \sim 2$ studied by Erb et al. (2006), who find a mean inferred gas mass is $\langle M_{\rm gas}\rangle = (2.1 \pm 0.1) \times 10^{10}\,M_\odot$. We estimate the gas fraction of DLA 2222−0946, calculated as $f_{\rm gas} = (M_{\rm gas}/(M_{\rm gas} + M_{\rm dyn}))$, to be $f_{\rm gas} \sim 40\%$, in agreement with the Krogager et al. (2013) estimate.

4.3. Morphology and Kinematics

A comparison of the Hα and [N II] emission maps, shown in Figures 4 and 5, reveals much information about the morphological and kinematical state of DLA 2222−09. First,

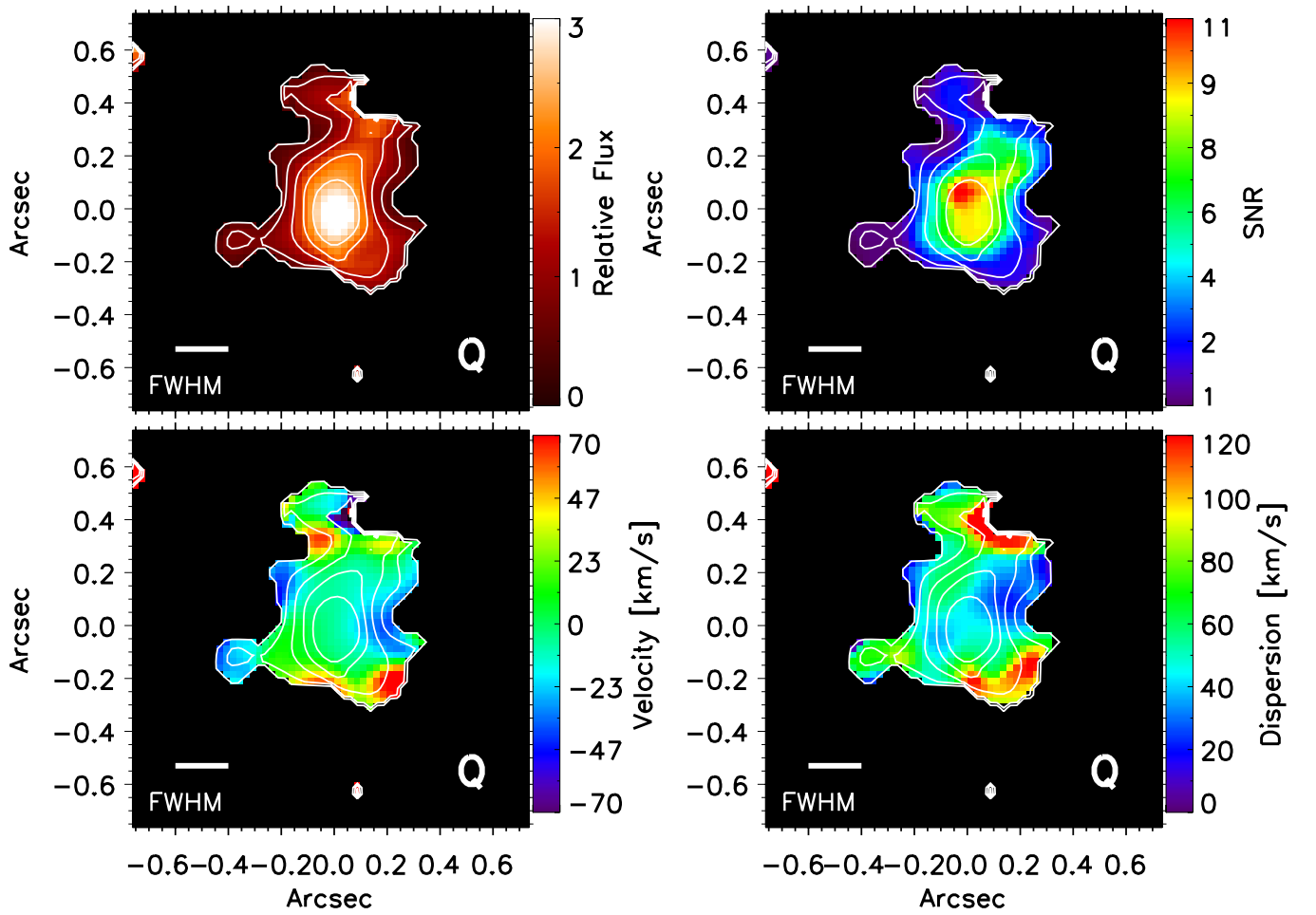

Figure 5. [O III] λ5007 intensity (top left), velocity (bottom left), velocity dispersion (bottom right), and S/N (top right) maps. The orientation is the standard north is up and east is to the left. The velocity is relative to $z = 2.35397$, the best-fit redshift determined from the composite spectrum shown in Figure 3. Individual spaxels are 0.025 arcsec^2. The FWHM = ∼0.″20 of the PSF after smoothing is shown in the lower left corner of the intensity map. At the redshift of the DLA 1″ corresponds to ∼8.3 kpc. The quasar, indicated by a "Q," is located in the lower right-hand corner at approximately $x = 0.''5$ and $y = -0.''6$.

(A color version of this figure is available in the online journal.)

we find that while the peak Hα and [O III] emission correspond spatially, the [O III] emission is stronger and slightly more spatially extended than that of the Hα. In both cases, the roughly circular morphology makes it difficult to determine a potential kinematic major axis, and suggests a face-on disk orientation. The velocity profiles, shown in the bottom left of Figures 4 and 5, reinforce this picture, as there is no clear kinematic signature of rotation. While we do detect some "clumps" of red and blue shifted emission, the velocity across the central emission region, as seen in both the Hα and [O III] velocity maps, appears relatively constant.

In the most simplistic approximation, we can estimate the amount of dynamical support provided by rotation by calculating $v_{\rm shear}/\sigma_{\rm mean}$, where the velocity shear, $v_{\rm shear} = (1/2)(v_{\rm max} - v_{\rm min})$, and $\sigma_{\rm mean}$ is the mean velocity dispersion of the system. We find $v_{\rm shear} = 119 \pm 11$ km s^{-1}, and $\sigma_{\rm mean} \sim 57$ km s^{-1}, resulting in $(v_{\rm shear}/\sigma_{\rm mean}) \sim 2.1$. However, we caution that while this seems to be indicative of a rotationally supported disk (i.e., Förster Schreiber et al. 2009a; Law et al. 2009), these values were derived by averaging over the system as a whole, and we do not see evidence of the classical, edge-on disk rotation in which the velocity dispersion should peak at the center of rotation. Our result is consistent with that of Peroux et al. (2013) who find this system to be dispersion dominated.

To quantitatively search for signs of edge-on disk rotation, we created artificial slits and extracted the velocity and velocity dispersion, σ. The slit widths were made to match the FWHM of the seeing, 0.″15. We then placed the slit on the region of interest and extracted the median velocity and σ over dispersion regions equal to 1/2 of the FWHM, or 0.″075. For example, in Figure 6, top, we place the slit at position angle (PA) ∼ 70° east of north, and find that the velocity and velocity dispersion are indicative of an edge-on disk rotation pattern in which the velocity smoothly varies from +50 km s^{-1} to −50 km s^{-1} across the span of ∼5 kpc while the corresponding velocity dispersion peaks in the middle at $v = 0$ km s^{-1} relative velocity and $\sigma \sim 120$ km s^{-1}. However, despite the intriguing kinematic possibility, we doubt the interpretation of this as disk rotation because (1) the center of rotation is not aligned with the peak of Hα emission, as would be expected, and (2) the large σ and relatively small velocity shear would indicate a dispersion dominated system rather than a large, rotationally supported disk. In Figure 6, bottom, we align the slit at PA ∼ 15° west of north to demonstrate how a velocity profile that seems indicative of rotation is clearly not when the associated velocity dispersion is examined.

While there is no clear evidence of disk-like morphology or rotation, we note that the kinematic signatures that are seen, agree, at least qualitatively, across the independent Hα and

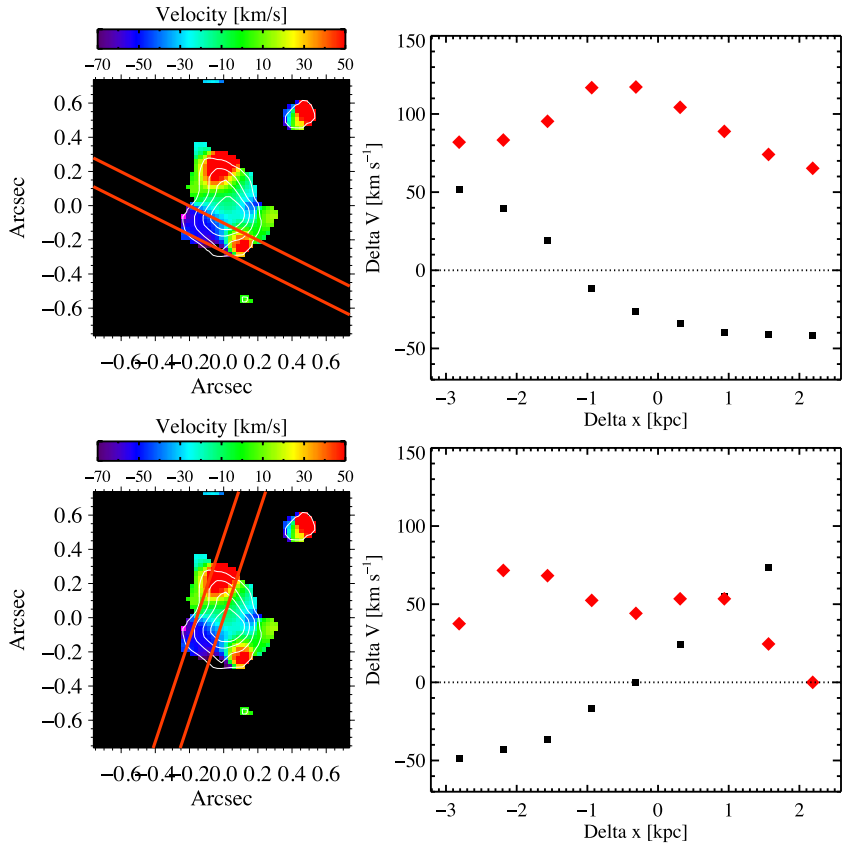

Figure 6. Laying down artificial slits on the Hα emission map. Relative velocity (black squares) and velocity dispersion (red diamonds) extracted from the slit are plotted on the right, where the *x*-axis is position along the slit in kiloparsecs, while the *y*-axis is the velocity difference from the central redshift.
(A color version of this figure is available in the online journal.)

[O III] emission-line maps. For example, both the Hα and [O III] velocity maps show regions of redshifted emission both north and south of the central emission peak, while blueshifted regions appear along a roughly east-west axis. Interestingly, these blueshifted regions appear, at least qualitatively, to align with the major axis of rest-frame UV emission detected by Krogager et al. (2013). From their *HST* F606W image, Krogager et al. (2013) find that DLA 2222−0946 has a compact, elongated structure indicative of an edge-on disk. Given that both Hα and the rest-frame UV should trace the sites of active star formation, it is not clear why the galaxy morphology implied by the *HST* image and the Hα emission map presented here, should be different. One explanation may be that foreground dust, perhaps associated with the blueshifted Hα emission, is obscuring background UV emission, causing the appearance of an elongated, disk-like morphology in the rest-frame UV. Another possible interpretation may be a bipolar outflow scenario akin to that found in M82 which creates the slightly red and blue shifted emission above and below the disk, respectively. However, given the generally low S/N of these blue and redshifted regions (S/N $\lesssim 2$), we are hesitant to over-interpret their significance or meaning.

4.4. Evidence of Metallicity Gradient or Metal-enriched Winds/outflow/infall?

The relatively high metallicities of DLAs compared with the Lyα forest (Schaye et al. 2003; Aguirre et al. 2004), in addition to the Hubble Deep Field constraint on in situ star formation (Wolfe & Chen 2006; Rafelski et al. 2011), suggest that metal enrichment of DLAs is at least partially due to a secondary process such as the ejection and infall of metal-enriched winds. The observations of DLA 2222−0946 presented here may support just such a scenario. The emission-line metallicity measured at the center of DLA 2222−0946, 75% solar, is more than twice as large as the metallicity determined from the absorption-lines, ∼30% solar, measured ∼6 kpc away in front of the background quasar. While the errors inherent in the emission-line derived metallicity via the $N2$ relation are large and these metallicities could be consistent with one another, we note that this could also be evidence of either a metallicity gradient in the galaxy, or the presence of metal-enriched winds escaping (or falling back onto) the galaxy.

4.5. Comparison with Keck/HIRES Absorption-line Data

In this section, we compare the OSIRIS data with a Keck/HIRES echelle spectrum of DLA 2222−0946 obtained from the Keck Observatory Archive. The spectrum was taken on 2006 August 17 with the C1 decker for a spectral resolution of ∼6 km s^{-1}. The final spectrum, a co-add of two 5400 s exposures for a total exposure time of 10,800 s, has a median S/N of ∼16 pixel^{-1}.

As reported in Jorgenson et al. (2013a), the metallicity as measured from the HIRES spectrum is [M/H] = −0.56 ± 0.10, which corresponds to a metallicity of ∼30% solar. The velocity interval containing 90% of the integrated optical depth of the low-ion metallic gas (Prochaska & Wolfe 1997) is also relatively large at Δv_{90} = 179 km s^{-1}. Similarly, the equivalent width of the Si II λ1526 line, thought to be a proxy for mass (Prochaska et al. 2008), is on the high end of DLA samples at

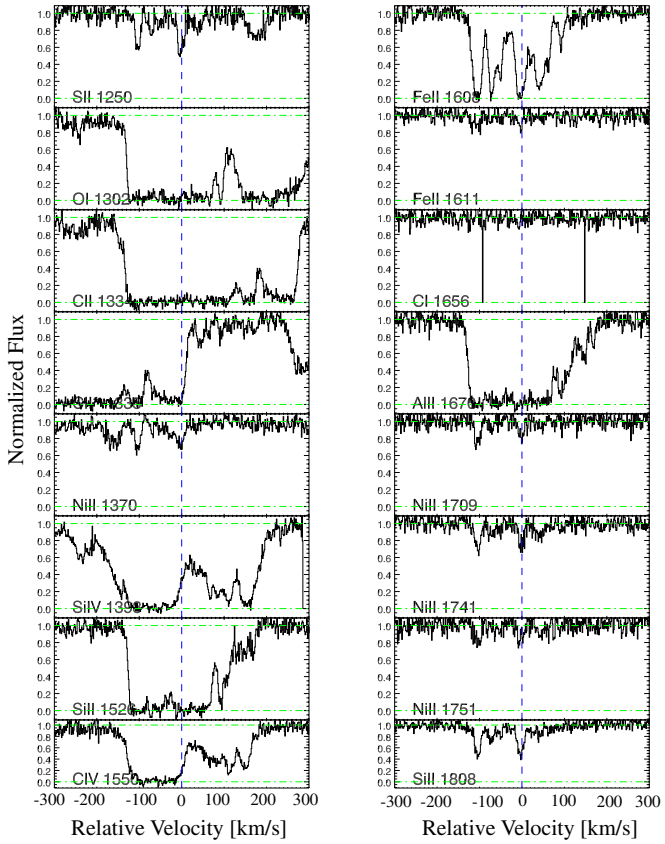

Figure 7. Select low- and high-ion velocity transitions from the Keck/HIRES spectrum. The velocity $v = 0$ km s^{-1} shown here corresponds to the fiducial redshift, taken to be $z_{\rm HIRES} = 2.35440$. For comparison, on this velocity scale, the peak of Hα emission falls at -44 km s^{-1}.

(A color version of this figure is available in the online journal.)

$W_{1526} = 1.23$ Å (Jorgenson et al. 2013a). Unfortunately, it is not possible to measure the level of star formation activity via the C II* technique (Wolfe et al. 2003), as the C II* λ1335.7 absorption-line is blended with the strong C II λ1334 line. However, all previously mentioned quantities, including metallicity, low-ion velocity width, and the Si II λ1526 equivalent width, indicate that DLA 2222−0946 is a typical "high-cool" DLA in which one might expect heating to be derived primarily from a nearby LBG galaxy (Wolfe et al. 2008).

In Figure 7, we present a selection of low- and high-ion velocity profiles of DLA 2222−0946. We arbitrarily define the fiducial absorption redshift of the system, $z_{\rm HIRES} = 2.35440$, to be located at the central, low-ion velocity component of highest optical depth, denoted by $v = 0$ km s^{-1}. As seen from the unsaturated species, e.g., Si II λ1808 and Si II λ1250, there is a second velocity component of high optical depth located at $v \sim -100$ km s^{-1}. Interestingly, the central redshift of the emission-lines, both Hα and [O III], places them at $v \sim -50$ km s^{-1}, in the middle of the two strongest low-ion velocity components. This remarkable coincidence between the emission-line redshift and the absorption-line redshift, measured ∼6 kpc away, was noted by Fynbo et al. (2010), who suggest it could be explained by the quasar line of sight passing parallel to the rotation axis of a face-on disk. In addition, we see that the high-ionization lines, such as C IV λ1550 and Si IV λ1393, have velocity profiles nearly identical to those of the low ions, with just slightly stronger redshifted velocity components. This is unusual for DLA velocity profiles, in which the high ions typically contain velocity components that are offset and extended in comparison with the low-ionization lines, and as a result thought to be tracing winds/outflows.

While it may be purely coincidental given the 6 kpc spatial separation, we note that the red and blue shifted emission clumps are shifted to velocities corresponding to the two highest optical depth low-ion absorption lines at $v \sim 0$ and $v \sim -100$ km s^{-1}. In Figure 8, we compare sub-stacks of Hα emission from spatial regions that appeared either blue or redshifted with respect to the central emission velocity, with the velocity profile of the unsaturated Si II λ1808 absorption feature. There exists a remarkable agreement between the redshifts (or velocities) of the emission sub-clumps and the two strongest low-ion absorption components. In the top and lower right panel, the best-fit redshift of the sub-stack Hα emission corresponds almost exactly with that of the Si II λ1808 velocity component at $v = 0$ km s^{-1}, while in the lower left panel, the best-fit Hα emission-line corresponds to within the errors with the Si II λ1808 velocity component at $v \sim -100$ km s^{-1}.

4.5.1. Molecular Hydrogen

Given the high metallicity and relatively large star formation rate of DLA 2222−0946, one might expect to detect a large amount of molecular gas. However, this gas is not detected in the HIRES spectrum. Using the HIRES spectrum, Jorgenson et al. (2013b) place an upper limit on the amount of molecular hydrogen (H_2) in the system, of $N(H_2) \lesssim 2 \times 10^{14}$ cm^{-2}. This corresponds to the low molecular fraction of $f \lesssim 10^{-5.8}$. In addition, there is no evidence of neutral carbon (C I) absorption, a species that is often associated in DLAs with the cold, dense gas required for the presence of H_2 (Jorgenson et al. 2010). While it is clear that there is not much, if any, H_2 in this DLA, the Hα emission indicates a SFR of $\sim 10\,M_\odot$ yr^{-1}. Presumably, H_2 had to exist at some point in order to create the stars producing the Hα emission. Is it merely chance that the sight line probed by the background quasar is devoid of molecules? Or is the molecular gas more centrally concentrated resulting in the apparently low H_2 covering factor found by surveys for H_2 (Jorgenson et al. 2013b)? Or could this be an example of a metal-rich, star-forming DLA galaxy in which copious star formation has temporarily depleted the supply of molecular gas? Follow up observations to search for molecular emission might help answer these questions.

4.5.2. Lyα emission

Strong asymmetric Lyman−α emission in the trough of DLA 2222−0946 is detected by Fynbo et al. (2010) and Krogager et al. (2013), with a flux of $F(\text{Ly}\alpha) = (14.3 \pm 0.3) \times 10^{-17}$ erg s^{-1} cm^{-2}. However, we do not detect Lyα emission in the HIRES spectrum. This is likely due to an unfortunate positioning of the slit during the Keck/HIRES observations. However, we do find evidence of a slight rise in the zero level on the red side of the DLA trough that is consistent with the Lyα emission profile as shown in Krogager et al. (2013).

5. SUMMARY

We present the first Keck/OSIRIS IFU observations of a high-redshift DLA galaxy that, aided by LGSAO, spatially resolve the Hα and [O III] emission. With a star formation rate of nearly $10\,M_\odot$ yr^{-1}, and a dynamical mass, $M_{\rm dyn} = 6.1 \times 10^9\,M_\odot$, DLA 2222−0946 appears similar to the low-mass end of the high-redshift star forming galaxies studied by Law et al. (2009).

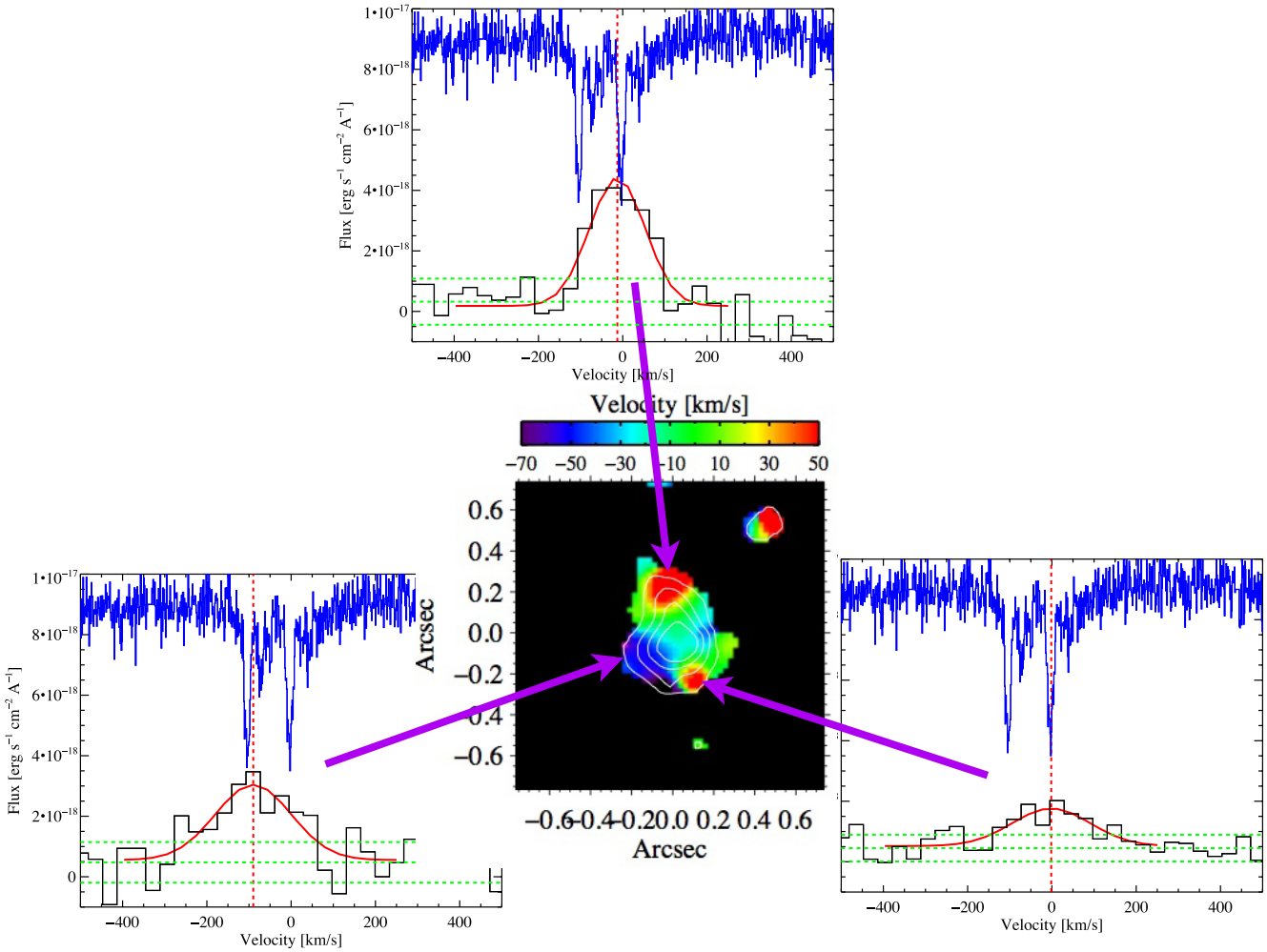

Figure 8. Hα emission profiles over small spatial regions compared with the Keck/HIRES spectrum of Si II λ1808 line (overplotted in blue). It is seen that the blue-shifted Hα region (lower left) corresponds in velocity space to the blue low-ion velocity component seen in the Keck/HIRES spectrum (here, at $v \sim 100$ km s^{-1}). Similarly, the redshifted Hα regions (top and lower right) closely correspond in velocity space to the red low-ion velocity component, here at $v \sim 0$ km s^{-1}.

(A color version of this figure is available in the online journal.)

We detect [N II] emission with 3σ significance and estimate a metallicity of 75% solar in the central galactic region. When compared with the absorption-line metallicity, ∼30% solar, measured 6 kpc away, this may suggest either a metallicity gradient or the presence of metal enriched out/inflow.

Kinematically, we find the central emission regions of maximum flux and S/N to be relatively constant, showing no evidence of a smoothly varying velocity gradient consistent with the rotation of a disk viewed edge-on, as suggested by the HST rest-frame UV images of Krogager et al. (2013). We do detect several red and blueshifted "clumps" of emission which could be analogous to the kiloparsec-sized clumps commonly seen in high-redshift star forming galaxies, e.g., Elmegreen et al. (2009a, 2009b). The lack of evidence of ordered rotation, in addition to the generally circular morphology indicated by the emission lines and the remarkable coincidence of emission and absorption-line redshifts, support the interpretation, originally proposed by Fynbo et al. (2010), that DLA 2222−0946 is a disk viewed nearly face-on. However, given the UV morphology detected by Krogager et al. (2013), we conclude that neither simple interpretation, of an edge-on or face-on disk, is consistent with all of the current observational data and that further clarity will likely require additional observations.

The observations presented here highlight the potential for using LGSAO+IFU instruments on 10 m class telescopes to finally achieve the long-sought goal of imaging the host galaxies of DLAs. We have demonstrated that it is possible, with reasonable exposure times of a few hours per object, to detect and map the relatively faint DLA emission around a bright, central quasar. Only by now increasing the sample of mapped DLA emitters will we finally be able to craft a better understanding of the nature of these elusive DLA systems and their role in galaxy formation and evolution.

We thank David Law, Tiantian Yuan, Randy Cambell, Jim Lyke, and Jessica Lu for many beneficial discussions, John O'Meara for providing the HIRES spectrum, and Jeff Cooke for providing comments on an early draft. We also thank the anonymous referee for a careful reading of the paper and many useful comments. R.A.J. gratefully acknowledges support from the NSF Astronomy and Astrophysics Postdoctoral Fellowship under award AST-1102683. The authors wish to recognize and acknowledge the very significant cultural role and reverence that the summit of Mauna Kea has always had within the indigenous Hawaiian community. We are most

fortunate to have the opportunity to conduct observations from this mountain.

REFERENCES

Adelberger, K. L., Erb, D. K., Steidel, C. C., et al. 2005, ApJL, 620, L75
Aguirre, A., Schaye, J., Kim, T., et al. 2004, ApJ, 602, 38
Asplund, M., Grevesse, N., Sauval, A. J., Allende Prieto, C., & Kiselman, D. 2004, A&A, 417, 751
Bouché, N., Murphy, M. T., Kacprzak, G. G., et al. 2013, Sci, 341, 50
Bouwens, R. J., Illingworth, G. D., Thompson, R. I., et al. 2004, ApJL, 606, L25
Bunker, A. J., Warren, S. J., Clements, D. L., Williger, G. M., & Hewett, P. C. 1999, MNRAS, 309, 875
Chabrier, G. 2003, PASP, 115, 763
Chengalur, J. N., & Kanekar, N. 2002, A&A, 388, 383
Christensen, L., Noterdaeme, P., Petitjean, P., Ledoux, C., & Fynbo, J. P. U. 2009, A&A, 505, 1007
Cooke, J., Wolfe, A. M., Gawiser, E., & Prochaska, J. X. 2006, ApJ, 652, 994
Cooke, J., Wolfe, A. M., Prochaska, J. X., & Gawiser, E. 2005, ApJ, 621, 596
Ellis, R. S., McLure, R. J., Dunlop, J. S., et al. 2013, ApJL, 763, L7
Elmegreen, B. G., Elmegreen, D. M., Fernandez, M. X., & Lemonias, J. J. 2009a, ApJ, 692, 12
Elmegreen, D. M., Elmegreen, B. G., Marcus, M. T., et al. 2009b, ApJ, 701, 306
Erb, D. K., Steidel, C. C., Shapley, A. E., et al. 2006, ApJ, 646, 107
Förster Schreiber, N. M., Genzel, R., Bouché, N., et al. 2009a, ApJ, 706, 1364
Fynbo, J. P. U., Laursen, P., Ledoux, C., et al. 2010, MNRAS, 408, 2128
Genzel, R., Tacconi, L. J., Eisenhauer, F., et al. 2006, Natur, 442, 786
Giavalisco, M., Dickinson, M., Ferguson, H. C., et al. 2004, ApJL, 600, L103
Haehnelt, M. G., Steinmetz, M., & Rauch, M. 1998, ApJ, 495, 647
Hinshaw, G., Larson, D., Komatsu, E., et al. 2013, ApJS, 208, 19
Hong, S., Katz, N., Davé, R., et al. 2010, arXiv:1008.4242
Jorgenson, R. A., Murphy, M. T., & Thompson, R. 2013a, MNRAS, 435, 482
Jorgenson, R. A., Murphy, M. T., Thompson, R., & Carswell, R. 2013b, MNRAS, submitted
Jorgenson, R. A., Wolfe, A. M., & Prochaska, J. X. 2010, ApJ, 722, 460
Kennicutt, R. C., Jr. 1998, ApJ, 498, 541
Kennicutt, R. C., Jr., Tamblyn, P., & Congdon, C. E. 1994, ApJ, 435, 22
Krogager, J.-K., Fynbo, J. P. U., Ledoux, C., et al. 2013, MNRAS, 433, 3091
Krogager, J.-K., Fynbo, J. P. U., Møller, P., et al. 2012, MNRAS, 424, L1
Kulkarni, V. P., Hill, J. M., Schneider, G., et al. 2000, ApJ, 536, 36
Kulkarni, V. P., Woodgate, B. E., York, D. G., et al. 2006, ApJ, 636, 30
Larkin, J., Barczys, M., Krabbe, A., et al. 2006, Proc. SPIE, 6269, 62691A
Law, D. R., Shapley, A. E., Steidel, C. C., et al. 2012, Natur, 487, 338
Law, D. R., Steidel, C. C., Erb, D. K., et al. 2007, ApJ, 669, 929
Law, D. R., Steidel, C. C., Erb, D. K., et al. 2009, ApJ, 697, 2057
Lehnert, M. D., Nesvadba, N. P. H., Cuby, J.-G., et al. 2010, Natur, 467, 940
Lowenthal, J. D., Hogan, C. J., Green, R. F., et al. 1995, ApJ, 451, 484
Newman, S. F., Genzel, R., Förster Schreiber, N. M., et al. 2013, ApJ, 767, 104
Peroux, C., Bouche, N., Kulkarni, V. P., & York, D. G. 2013, MNRAS, 436, 2650
Péroux, C., Bouché, N., Kulkarni, V. P., York, D. G., & Vladilo, G. 2011, MNRAS, 410, 2251
Péroux, C., Bouché, N., Kulkarni, V. P., York, D. G., & Vladilo, G. 2012, MNRAS, 419, 3060
Pettini, M., & Pagel, B. E. J. 2004, MNRAS, 348, L59
Prochaska, J. X., Chen, H.-W., Wolfe, A. M., Dessauges-Zavadsky, M., & Bloom, J. S. 2008, ApJ, 672, 59
Prochaska, J. X., & Wolfe, A. M. 1997, ApJ, 487, 73
Prochaska, J. X., & Wolfe, A. M. 2010, arXiv:1009.3960
Rafelski, M., Wolfe, A. M., & Chen, H.-W. 2011, ApJ, 736, 48
Rafelski, M., Wolfe, A. M., Prochaska, J. X., Neeleman, M., & Mendez, A. J. 2012, ApJ, 755, 89
Reddy, N. A., & Steidel, C. C. 2009, ApJ, 692, 778
Schaye, J., Aguirre, A., Kim, T., et al. 2003, ApJ, 596, 768
Schulze, S., Fynbo, J. P. U., Milvang-Jensen, B., et al. 2012, A&A, 546, A20
Shapley, A. E., Erb, D. K., Pettini, M., Steidel, C. C., & Adelberger, K. L. 2004, ApJ, 612, 108
Steidel, C. C., Adelberger, K. L., Giavalisco, M., Dickinson, M., & Pettini, M. 1999, ApJ, 519, 1
Steidel, C. C., Adelberger, K. L., Shapley, A. E., et al. 2003, ApJ, 592, 728
Wolfe, A. M., & Chen, H. 2006, ApJ, 652, 981
Wolfe, A. M., Gawiser, E., & Prochaska, J. X. 2005, ARA&A, 43, 861
Wolfe, A. M., Prochaska, J. X., & Gawiser, E. 2003, ApJ, 593, 215
Wolfe, A. M., Prochaska, J. X., Jorgenson, R. A., & Rafelski, M. 2008, ApJ, 681, 881
Wolfe, A. M., Turnshek, D. A., Smith, H. E., & Cohen, R. D. 1986, ApJS, 61, 249